Journal of Colloid and Interface Science 691 (2025) 137409

Contents lists available at ScienceDirect

Journal of Colloid And Interface Science

journal homepage: www.elsevier.com/locate/jcis

Phase-engineered metal boride nanobeads for highly efficient oxygen evolution

Meijia Liu [a,1], Lin Wu [a,1], Yafeng Li [a], Shuai Chen [a], Yuhang Lei [a], Zhuang Huo [a], Lin Tao [a], Lixiang Li [a], Chengguo Sun [a,b], Han Zhang [a,*], Baigang An [a,*]

[a] Key Laboratory of Energy Materials and Electrochemistry Research Liaoning Province, School of Chemical Engineering, University of Science and Technology Liaoning, Anshan 114051, China

[b] School of Chemical Engineering, Nanjing University of Science and Technology, Nanjing 210094, China

GRAPHICAL ABSTRACT

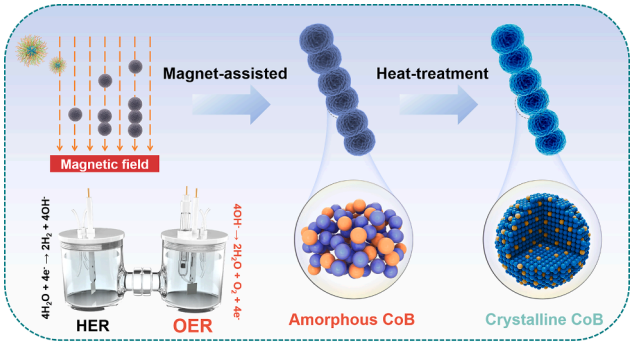

ARTICLE INFO

Keywords:
Magnetic field-assisted
Nanobead structure
Controlled phase
Amorphous
Self-reconstruction

ABSTRACT

Non-precious metals with tailored phase structures show promise as oxygen evolution reaction (OER) catalysts due to their high inherent catalytic activity and extensive exposed active surface area. However, the mechanisms by which phase structures enhance catalytic performance remain unclear. Herein, we synthesized an amorphous cobalt boride (CoB) catalyst via a magnetic field-assisted method, yielding uniform nanoparticles that self-assemble into a nanobead structure. This material undergoes heat treatment to transition from an amorphous phase to a crystalline phase. The catalyst demonstrated exceptional OER activity and long-term stability in an alkaline electrolyte, requiring only 350 mV overpotential at 10 mA cm^{-2}. The amorphous CoB demonstrates remarkable durability by maintaining stable operation for 100 h under harsh conditions characterized by high alkalinity and elevated temperature without any observable performance degradation. We demonstrate that electrochemical activation of an amorphous catalyst can unveil active sites within the bulk material, leveraging the short-range order characteristic of amorphous structures. This process significantly amplifies the active site density, consequently enhancing the electrocatalytic performance of the amorphous catalyst in the oxygen evolution reaction within water oxidation. Furthermore, in situ Raman spectroscopy reveals that amorphous CoB rapid self-reconstruction upon electrochemical activation, leading to the formation of a metal (oxy)hydroxide

* Corresponding authors.
[1] These authors contributed equally to this work.

https://doi.org/10.1016/j.jcis.2025.137409
Received 26 December 2024; Received in revised form 19 March 2025; Accepted 20 March 2025
Available online 21 March 2025

active layer. This study offers valuable insights into the design of high-efficiency OER catalysts by elucidating the mechanisms underlying amorphous and crystalline materials.

1. Introduction

In order to combat the issues of the energy crisis and environmental degradation, as well as to overcome reliance on finite fossil fuels, there is a growing need for clean and renewable energy [1]. Hydrogen, a rich source of green and versatile secondary energy, has been widely studied as a substitute for fossil fuels. Hydrogen boasts several advantages: high calorific value, good combustibility, produces only water upon combustion, and offers various methods for production, storage, and transportation [2]. Electrochemical and photochemical water splitting into hydrogen and oxygen has been considered a potential green hydrogen preparation technology. However, the conversion of solar energy to hydrogen is less efficient during photochemical water electrolysis [3]. It is well known that water splitting consists of two half-reactions: the hydrogen evolution reaction (HER) on the cathode side and the oxygen evolution reaction (OER) on the anode side. The kinetics of the oxygen reaction in these processes are extremely slow, which severely hampers the energy conversion efficiency [4–6]. To achieve effective water splitting, a low-cost advanced material is required that can increase the reaction rate, lower the reaction barrier, and reduce the overpotential [7,8]. In recent years, several noble metals have been developed as catalysts for OER, including noble metal-based catalysts (e.g., Ir, Rh, Ru, Pd) and although they exhibit excellent OER performance during the reaction process, their high cost as well as scarcity make it impossible to be widely used, and therefore there is an urgent need to search for highly efficient and low-cost electrocatalysts [9,10].

Recent studies have focused on developing highly active non-precious metal-based catalysts as alternatives to precious metal catalysts [11]. Various design strategies have been proposed to enhance the performance of OER catalysts, including enhancing the intrinsic activity of active sites [12,13], and increasing their quantity. Additionally, controlling phase composition has been shown to improve the properties of energy materials for diverse applications, such as electrodes and catalysts. Amorphous-based electrocatalysts have demonstrated superior OER performance compared to their crystalline counterparts [14]. Amorphous materials have garnered significant interest in the field of electrocatalysis, particularly for water oxidation, where they demonstrate superior catalytic activity and lower overpotentials compared to crystalline materials [15,16]. The amorphous structure is posited to provide a greater number of active sites for the OER. Dau et al. [17] attributed the enhanced OER activity of electrodeposited amorphous CoCat films to the bulk oxide, while subsequent studies by Liu [18] and Menezes [19] linked the abundance of active sites to a high density of oxygen vacancies. In particular, transition metal borides have been shown to exhibit high OER activity. Moderately electronegative boron ($\chi_{Pauling} = 2.04$) reduces the energy barrier for metal oxidation reactions and facilitates charge transfer, leading to improved OER performance in metal borides and borates [20]. In metal borides (M_xB), boron not only enhances the stability of the M_xB phase but also significantly boosts the catalytic activity of amorphous metal borides [21]. The improved catalytic activity of amorphous-phase electrocatalysts can be attributed to several factors: Firstly, structural and chemical disorder, enabling amorphous catalysts to be fully catalytically active, in contrast to crystalline catalysts that are predominantly surface-active; Secondly, high density of defects and dangling bonds, which substantially enhances the intrinsic catalytic activity and electrochemical stability of amorphous materials. Thirdly, structural flexibility, allowing for the in situ transformation of initially inert species into catalytically active phases during the reaction process [22,23]. Given these advantages, amorphization offers a promising approach to overcome the slow kinetics of OER in rigid crystalline catalysts, leading to improved electrochemical water-splitting performance [24,25]. Therefore, the development of effective amorphous catalysts is essential for addressing the challenge of slow OER kinetics in hydrogen production through water electrolysis [26–28]. However, the precise mechanisms by which amorphous catalysts surpass their crystalline counterparts in performance remain a subject of debate. Furthermore, the long-term operational stability of amorphous catalysts under the conditions required for practical water electrolysis, such as elevated overpotential and high current densities, is still questionable.

Herein, an amorphous metal boride catalyst was developed via a magnetic field-assisted method, featuring uniformly sized nanoparticles arranged in a nanobead structure, which facilitates bulk domain catalysis through structural defects inherent to the amorphous phase. Moreover, unlike the surface-limited catalysis of crystalline structures, the amorphous structure facilitates faster surface reconfiguration during catalytic reactions and ensures superior corrosion resistance. With a Tafel slope of 65.8 mV dec^{-1} and a current density of 10 mA cm^{-2} at 350 mV, the catalyst's characterization studies demonstrated its great stability and low overpotential. Remarkably, the material maintained its high catalytic activity even after 100 h of continuous OER. Thus, this study introduces a new strategy for designing electrocatalysts across a wide range of reactions.

2. Experimental section

2.1. Materials

Cobalt chloride hexahydrate ($CoCl_2{\cdot}6H_2O$, 99%), polyvinylpyrrolidone (PVP, 98%, M_w = 40,000), sodium borohydride ($NaBH_4$, 99%), ruthenium oxide (RuO_2, 99%), potassium hydroxide (KOH, 90%) were purchased from Aladdin Industries.

2.2. Synthesis of amorphous CoB

First, 47.6 mg of $CoCl_2{\cdot}6H_2O$ and 200 mg of PVP were dissolved in 50 mL of deionized water in three-necked round-bottom flask (the deionized water was purged with N_2 to remove air). Subsequently, the prepared $NaBH_4$ solution (25 mg in 20 mL) was added dropwise to the above solution. A fixed magnetic field strength of approximately 0.4 T was applied under the vessel. $NaBH_4$ solution was added drop by drop under an atmosphere of nitrogen and continuous stirring and the reaction process (10 min) was carried out under low temperature stirring. The synthesized black powdered material was collected by centrifugation and washed several times with large amounts of distilled water and ethanol respectively. The resulting sample was denoted as amorphous CoB.

2.3. Synthesis of crystalline CoB

The amorphous CoB was annealed for 2 h at 400°C (heating rate 5°C min^{-1}) under an argon atmosphere. The resulting CoB is referred to as crystalline CoB.

2.4. Synthesis of no magnet amorphous CoB

The synthesis process is similar to that of amorphous CoB, with the difference being that no magnetic field is placed under the three-necked round-bottom flask during the synthesis.

2.5. Structure characterization

The physical composition of the catalysts was examined by X-ray powder diffractometer (XRD, D8 ADVANCE). Field emission scanning electron microscopy (SEM, Thermo Fisher Scientific Apreos) and transmission electron microscopy (TEM, FEI Tecnai G2 F30) were used to acquire surface morphology. Using X-ray photoelectron spectroscopy (XPS, Kratos ASIS SUPRA), the materials' elemental composition and chemical valence were assessed. A confocal Raman microscope (HORIBA) equipped with a 50 × objective and an excitation wavelength of 532 nm was used to gather in situ Raman spectra. Measurements were taken at 0.05 V intervals in the potential range of 0–0.6 V (Ag/AgCl for the reference electrode and platinum foil for the counter electrode), with the grating parameter set at 600 GR mm^{-1} and the laser intensity set at 10 mW.

2.6. Electrochemical measurement

The electrochemical measurement tests were carried out in a standard three-electrode device system on a CHI660E electrochemical workstation. Ag/AgCl was used as the reference electrode, Pt foil as the counter electrode, and a glassy carbon electrode coated with a catalyst layer (6 mm in diameter with a surface area of 0.2826 cm^2) was used as the working electrode, and the potential value of the Ag/AgCl electrode was converted to the standard reversible hydrogen electrode E (vs. RHE) = E (vs. Ag/AgCl) + 0.198 + 0.059*pH, according to the formula. 5 mg of catalyst was dispersed in a mixture of deionized water (500 μL), ethanol (500 μL) and Nafion (50 μL, 5 wt%) to form a homogeneous catalyst ink. The catalyst ink (20 μL) was then dropped onto the working electrode. The catalyst ink was then spinning drop-casted (<700 rpm) onto the RDE electrode with a 0.24 mg_{cat} cm^{-2} loading amount for all samples. Sample OER tests were performed in alkaline electrolyte (1.0 M KOH) solution. With the reversible hydrogen electrode serving as the reference for all measured potentials, linear sweep voltammetry (LSV) was performed at a scan rate of 2 mV s^{-1}. Using the electric double layer capacitance (C_{dl}) from cyclic voltammetry (CV) in a non-Faradaic potential window, the electrochemical surface area (ECSA) was calculated. CV curves were captured throughout a potential range of 1.19 to 1.33 V vs RHE at scan rates between 10 and 50 mV s^{-1}. In order to conduct electrochemical impedance spectroscopy (EIS), a 5 mV AC signal was applied throughout a frequency range of 100 kHz–0.1 Hz. I–t curves were also obtained in order to assess the catalyst's long-term stability.

2.7. AEMWE operation

PiperlON A40-HCO_3 was used as the anion exchange membrane. The geometric area of electrode was 1 cm^2. The amorphous CoB/NF anode was fabricated by ink-spraying onto nickel paper. The E130 Raney nickel mesh, serving as the cathode, was utilized to construct the E130|| CoB/NF AEMWE (Alkaline Exchange Membrane Water Electrolyzer).

3. Results and discussion

We have prepared cobalt-based boride nanostructures using a simple and effective chemical reduction process. Fig. 1 illustrates the synthesis of amorphous cobalt-based boride nanobeads. First, Co^{2+} was chemically reduced in an ice-water bath using cobalt chloride hexahydrate and sodium borohydride as reducing agents. Polyvinylpyrrolidone (PVP) was adsorbed on the surface of the nanoparticles to form a protective layer that prevents agglomeration and helps in their dispersion [29]. Under a magnetic field, nanobeads align and attract each other along the field direction, attaching to particles with similar domains to form a dispersed structure, resulting in amorphous CoB. Crystalline CoB was subsequently obtained through heat treatment. The amorphous CoB was characterized by scanning electron microscopy (SEM). Fig. 2a and b show that the amorphous CoB consists of homogeneous nanorods with a size of 200–400 nm. The length of the nanochain is 2–4 μm. Under the influence of a magnetic field, these nanospheres are neatly aligned to form the morphology of magnetic nanobeads. On the contrary, the CoB material synthesized in the absence of a 400 mT magnet exhibits significant nanoparticle agglomeration as shown in Fig. S1. Amorphous nanobeads were successfully synthesized using a magnetic field-assisted method, which facilitated charge transfer, improved electrolyte penetration and diffusion, and promoted rapid gas release during the catalytic process [30,31].

Transmission electron microscopy (TEM) analysis revealed uniformly distributed nanoparticles with sizes between 200 and 300 nm (**Fig. S2**). Following annealing of amorphous CoB under argon at 400℃ for 2 h, the nanobead morphology and bead size remained unchanged, with uniform distribution of Co and B elements (**Fig. S3**). However, the B content decreased from 5.7 % to 2.4 %, likely due to B evaporation during the annealing process (**Table S1**) [32]. High-resolution transmission electron microscopy (HR-TEM) image (Fig. 2**d**) and selected area electron diffraction (SAED, inset of Fig. 2**d**) confirm the amorphous structure of CoB, consistent with the XRD patterns. The crystalline CoB retains nanobead morphology (Fig. 2**c**). As shown in Fig. 2**e**, the HR-

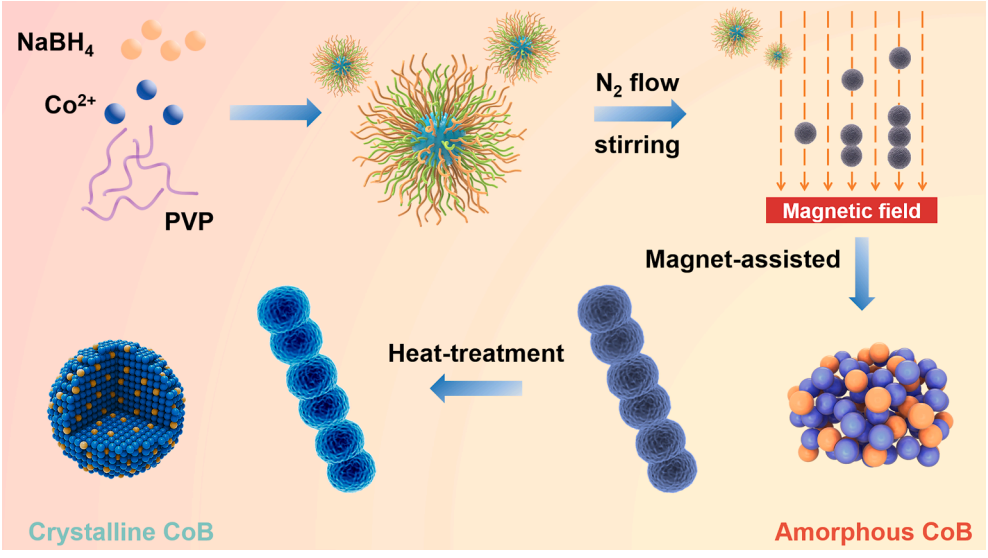

Fig. 1. Schematic diagram for the preparation amorphous CoB and crystalline CoB electrocatalyst.

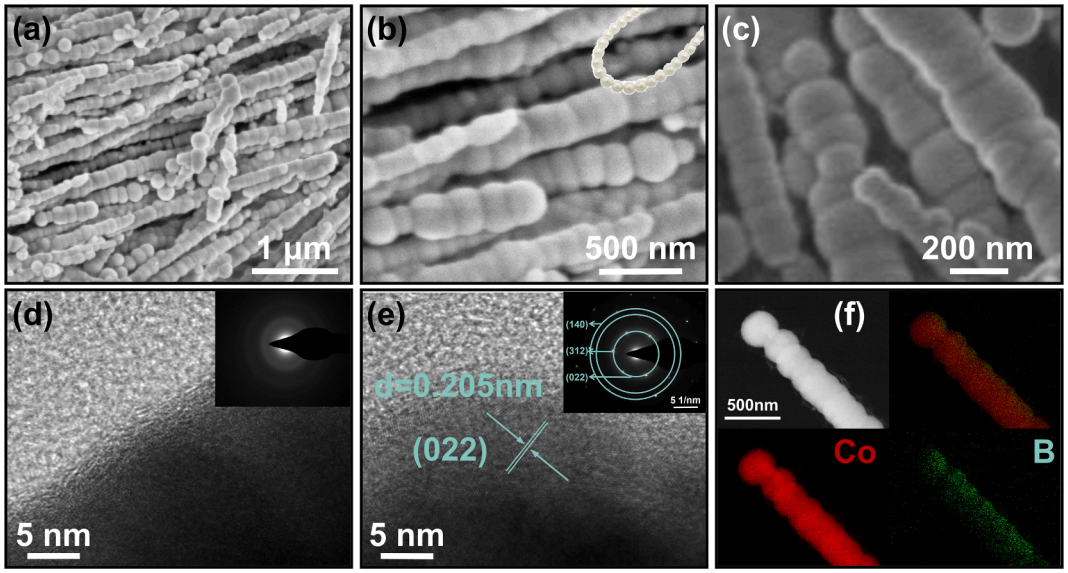

Fig. 2. SEM images of (a, b) amorphous CoB and (c) crystalline CoB. (d, e) HR-TEM image of amorphous CoB and crystalline CoB. (f) HAADF-STEM images of amorphous CoB and corresponding elemental mapping of Co and B.

TEM reveals lattice fringes with a spacing of 0.205 nm, corresponding to the (0 2 2) plane of Co_4B. The diffraction rings in the SAED image correspond to the (1 4 0), (3 1 2) and (0 0 2) crystal planes, with the (0 0 2) plane also visible in the lattice fringes, confirming the crystalline nature of annealed Co_4B. Energy dispersive X-ray spectroscopy (EDS) analysis indicated that the CoB catalyst contained Co and B elements, which were uniformly distributed (Fig. 2**f**).As shown in Fig. S4, amorphous CoB has good hydrophilicity with a contact angle of 60°, which is significantly smaller than that of crystalline CoB at 98°, which is more favorable for the adsorption of reagents on the cathode in the subsequent reaction and promotes mass transport in the kinetics of the electrocatalytic reaction.

The structure of the catalysts was examined by X-ray powder diffractometry (XRD). The XRD results showed no significant diffraction peaks for the amorphous CoB, indicating its amorphous form (Fig. 3**a**). The annealed crystalline CoB displayed distinct diffraction peaks corresponding to the (1 2 0), (0 2 2), (2 1 1), (3 1 2) and (1 4 0) crystal planes at 40.04°, 44.14°, 46.83°, 72.60° and 75.86°, respectively, of Co_4B (PDF#39-1107). This indicates the successful synthesis of CoB nanomaterials with crystalline structural features.

The types of vacancies in amorphous and crystalline CoB were further investigated using X-band electron paramagnetic resonance (EPR) spectroscopy (Fig. 3b). From the EPR spectrum of the CoB, it can be seen that a paramagnetic absorption signal at g = 2.003 can be attributed to the uncoordinated O vacancies on the surface. The amorphous CoB exhibits a stronger peak intensity, suggesting it can contain more oxygen vacancies to capture more electrons [33]. The chemical valence states of the elements were determined by X-ray photoelectron spectroscopy (XPS). The full spectrum of XPS shows that both amorphous and crystalline CoB catalysts comprise Co, B, C and O (Fig. 3**c**),

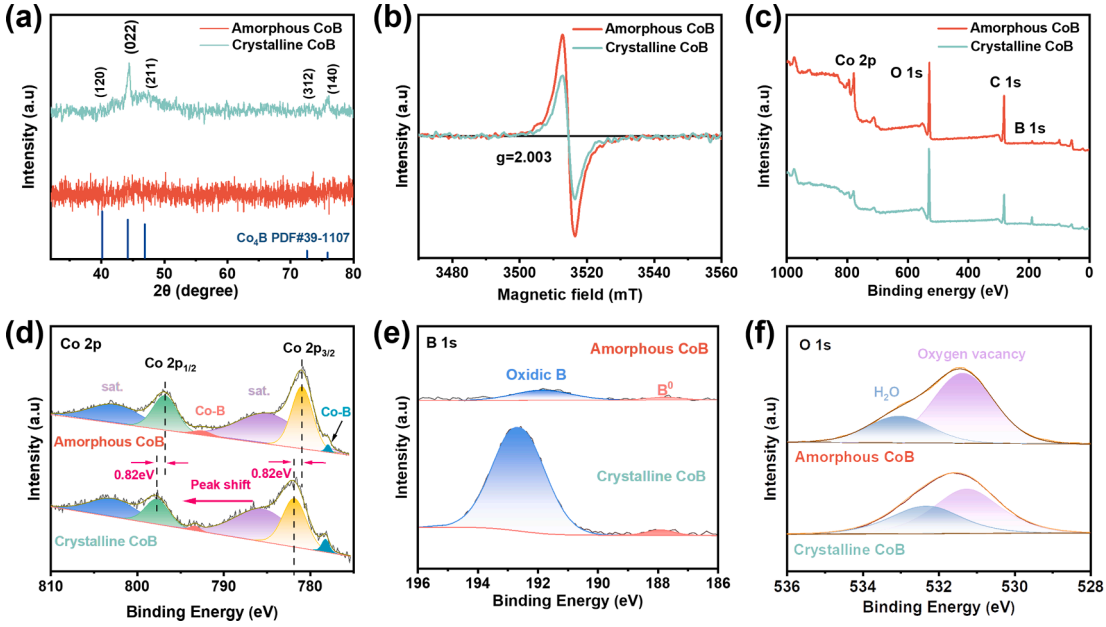

Fig. 3. (a) XRD patterns. (b) EPR spectra of amorphous CoB and crystalline CoB. (c) XPS spectra of survey. (d-f) High resolution Co 2p, B 1s and O 1s XPS spectra of amorphous CoB and crystalline CoB.

consistent with the EDS mapping results. For the Co 2p spectra (Fig. 3**e**), the peaks at 779.5 and 778.4 eV are attributed to the bonding of metallic Co with B. Additionally, the spectra in the Co 2p region show two spin–orbit double states for Co^{2+} at the Co $2p_{1/2}$ orbitals (796.8 eV) and at the Co $2p_{3/2}$ orbitals (781.0 eV), which is attributed to the oxidation of some of the Co by air to form cobalt oxide during the preparation [32]. The Co $2p_{3/2}$ peaks of amorphous CoB are shifted to higher binding energy by 0.82 eV compared to crystalline CoB, indicating an increase in the electron cloud density of Co after heat treatment (Fig. 3**d**) [34]. In Fig. 3**e**, both metallic boron (187.7 eV) and boron oxide (191.8 eV) are present in the B 1 s spectrum. Compared with amorphous CoB, the B_0 bonding peak in crystalline CoB is notably reduced (**Fig. S5**), likely due to B element loss during annealing, which corresponds to a decrease in B content [33]. Furthermore, the XPS spectra of O 1 s reveal two oxidation states in CoB (Fig. 3**f**). Peaks at 531.3 and 532.6 eV correspond to oxygen defects and physically/chemically adsorbed water, respectively. The higher oxygen vacancy concentration in amorphous CoB is attributed to its disordered atomic structure and oxygen removal by $NaBH_4$, which induces these vacancies. In contrast, high-temperature annealing facilitates atomic diffusion and covalent bond formation, thereby reducing oxygen vacancies during the preparation of crystalline CoB [34,35].

The prepared amorphous CoB, crystalline CoB and RuO_2 were tested for OER electrocatalytic activity in 1.0 M KOH solution using a standard three-electrode configuration [36]. At the current density of 10 mA cm^{-2}, an overpotential of 350 mV was needed for amorphous CoB (Figs. 4a and S6). By comparison, overpotentials were 384 mV for crystalline CoB and 443 mV for RuO_2. Notably, all cobalt boride-based samples showed higher catalytic activity compared to the commercial RuO_2 catalyst, which required 529 mV to reach a current density of 50 mA cm^{-2} (Fig. 4**c**), whereas amorphous CoB maintained the smallest overpotentials even at large current densities, compared to crystalline CoB and RuO_2 catalysts (**Fig. S7**). It exhibited the lowest Tafel slope of 65.8 mV dec^{-1}, outperforming both crystalline CoB (106.6 mV dec^{-1}) and RuO_2 (84.2 mV dec^{-1}). (Fig. 4**b**). Furthermore, the amorphous CoB outperformed the CoB catalyst synthesized without a magnetic field (**Fig. S8**). These results suggest that the short-range ordered, long-range disordered structure of the amorphous state enhances OER kinetics. This structural arrangement enables amorphous catalysts to drive overall catalysis, whereas crystalline catalysts are limited to surface catalysis [37,38].

The electrochemically active surface area (ECSA), reflecting the active sites of amorphous and crystalline CoB catalysts, was evaluated based on the double-layer capacitance (C_{dl}) calculated from cyclic voltammetry results. Since C_{dl} is directly proportional to ECSA, the results are shown in Figs. 4d and S9. The C_{dl} of amorphous CoB is 60.6 mF cm^{-2}, larger than that of crystalline CoB (49.8 mF cm^{-2}) and RuO_2 catalyst (1.6 mF cm^{-2}). It is also much larger than the CoB catalyst synthesized without a magnet (**Fig. S8**). These results indicate amorphous CoB catalysts have higher ECSA compared to their crystalline counterpart due to their abundance of surface defects and unique amorphous structure and hence more active sites [39,40].

Electrochemical impedance spectroscopy (EIS) was used to study the electrocatalytic reaction resistance in order to better explore the electrocatalytic kinetic properties of the catalysts. Nyquist plots were are

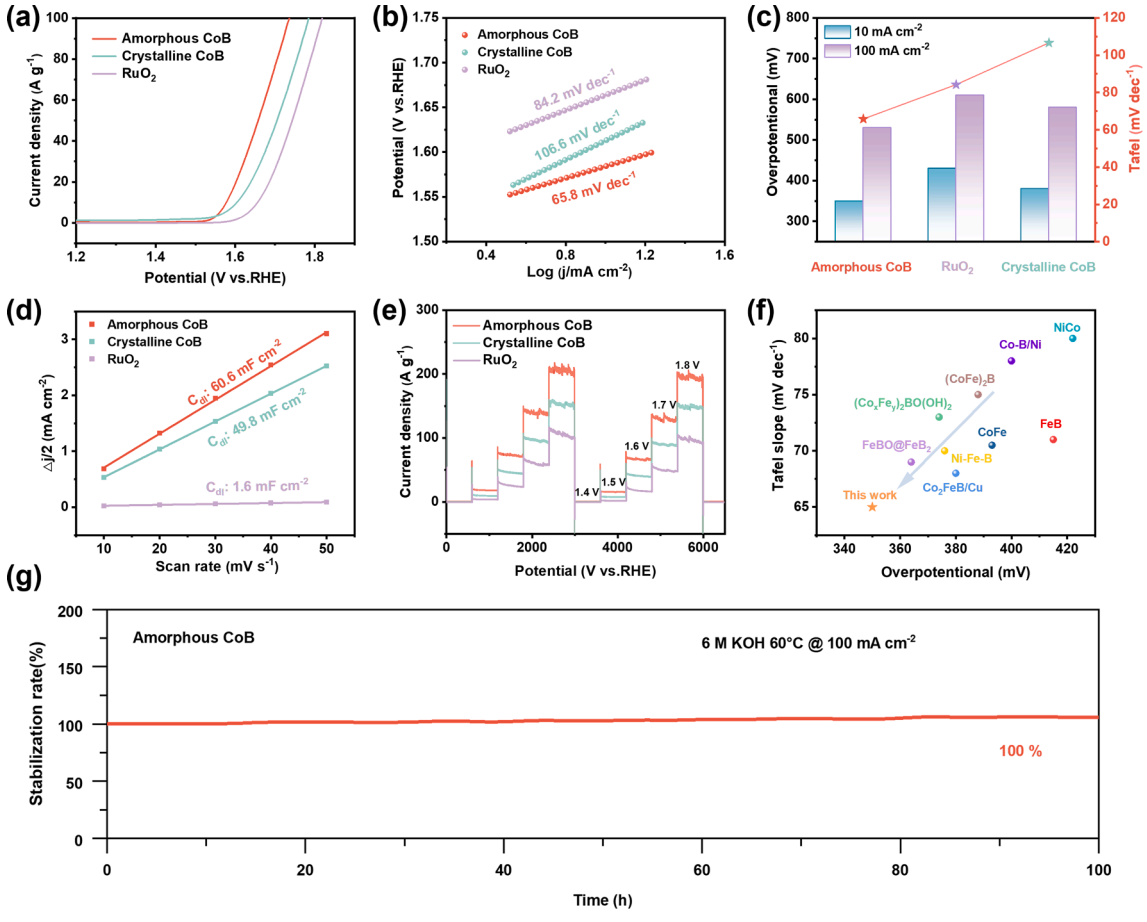

Fig. 4. (a) OER polarization curves, (b) Tafel plots obtained from OER polarization curves of amorphous and crystalline CoB and RuO_2. (c) Comparison of the overpotential, (d) Electrochemical double-layer capacitance (C_{dl}) of amorphous and crystalline CoB and RuO_2. (e) Multistep chronopotentiometry curves of amorphous and crystalline CoB and RuO_2. (f) Comparison of overpotentials and Tafel slopes of amorphous CoB catalysts in with existing reported OER catalysts. (g) Chronoamperometric durability test of amorphous CoB.

presented in **Fig. S10** and fitted with an equivalent circuit model for the quantification of the key kinetic parameter, the charge transfer resistance (R_{ct}). The fitting results show that the R_{ct} of amorphous CoB is smaller than that of crystalline CoB, confirming efficient electron transfer at the interface between the amorphous CoB catalyst electrode and electrolyte. In contrast, commercial RuO_2 catalysts showed large interfacial charge transfer resistance [41,42].

The durability and robustness of the amorphous and crystalline CoB were further evaluated by multi-step chrono-potential tests, and long-term bulk electrolysis. As shown in Figs. 4e and S11, after cycling the voltage between 1.4 and 1.8 V, the amorphous CoB exhibited a higher current density than both crystalline CoB and RuO_2 catalysts, reaching 180 mA cm^{-2} at 1.8 V. This value significantly surpassed that of crystalline CoB (120 mA cm^{-2}) and RuO_2 (80 mA cm^{-2}), with minimal fluctuation and stable catalyst performance. This suggests that amorphous CoB has good mass transfer performance and stability. Generally, the catalytic performance of amorphous CoB exceeds that of the crystalline form due to the presence of sufficient active sites. In addition, a comparison with the existing reported advanced OER catalysts reveals that amorphous CoB has the smallest Tafel slope and produces much lower overpotentials than other non-precious metal OER catalysts, indicating that the catalytic performance of amorphous CoB is superior to that of most of the previously reported catalysts [43]. Amorphous CoB exhibits superior water oxidation performance, significantly outperforming previous literature reports and transition metal-based catalysts (Fig. 4**f** and **Table S2**). To demonstrate the applied feasibility under the industrial conditions, the OER performance of amorphous CoB catalyst was further evaluated at 60°C in 6 M KOH. As shown in Fig. 4**g**, the amorphous CoB delivers a current densities retention exceeding 100 % and maintains its performance for 100 h under 100 mA cm^{-2}, showing its excellent stability in harsh industrial conditions. The results indicate that the activity and stability of amorphous CoB catalysts under alkaline conditions are superior to those of crystalline CoB. Additionally, LSV plots of the catalysts were recorded after long-term tests. The LSV curves after OER showed significant changes compared to the initial curves, with the overpotential of the amorphous CoB decreasing from 350 mV to 320 mV at 10 mA cm^{-2}. In contrast, the overpotential of crystalline CoB showed only a negligible change **(Fig. S12)**. Amorphous CoB undergoes rapid self-reconstruction during electrochemical activation, forming a metal (oxy)hydroxide active layer that serves as the active site for the OER [44].

In order to further identify the active catalytic sites during OER, we examined the surface chemistry and structural evolution of the catalysts after OER using SEM and in situ Raman spectroscopy analysis [44]. The SEM images in **Fig. S13** confirmed the evolution of the surface structure during the OER process, revealing surface self-reconstruction. After the reaction, the nanobeads retained their string-bead structure. To investigate catalyst activity enhancement and identify new surface substances after the OER, in situ Raman tests at various electrode potentials were conducted on amorphous CoB to clarify the OER mechanism and intermediate formation (Fig. 5**a**). Raman spectra obtained below 1.3 V revealed two weak peaks at 469 and 509 cm^{-1}, corresponding to the Co stretching (A_{1g}) and bending vibration features, respectively, while the 670 cm^{-1} peak is attributed to CoO_x. As the voltage increased, new peaks appeared at 601 and 718 cm^{-1}, corresponding to $Co(OH)_2$ and CoOOH, respectively. [45] The amorphous CoB acts as a precursor catalyst, transforming into $Co(OH)_2$ and CoOOH, which serve as active sites for the oxygen evolution reaction. In situ Raman spectroscopy

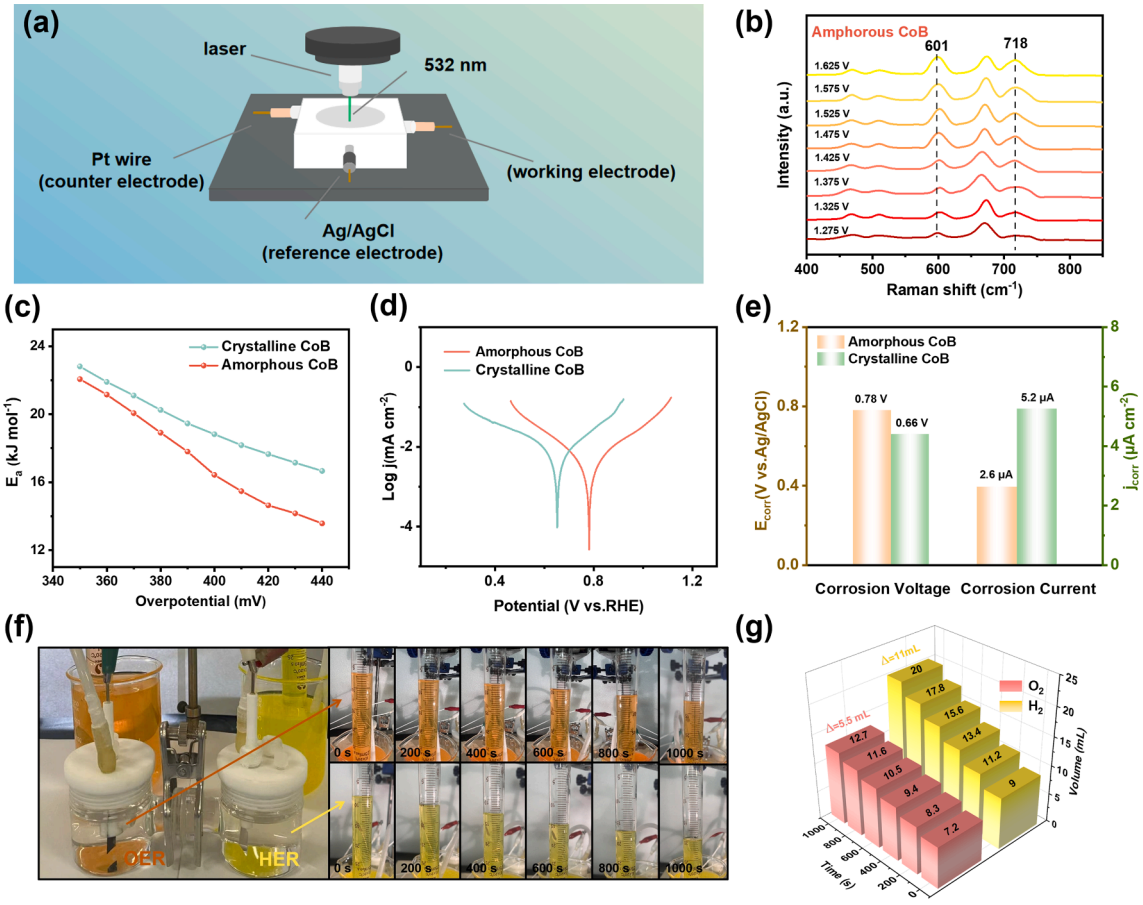

Fig. 5. Study of the surface reconstruction on amorphous CoB electrode during OER. (a and b) In situ Raman spectra of OER on amorphous CoB in 1 M KOH. (c) The E_a values of amorphous and crystalline CoB at different overpotential. (d and e) Corrosion polarization curve of various samples. (f) Reaction device of overall water splitting and the collected H_2 and O_2 volumes with time running. (g) Amount of O_2 and H_2 as a function of time at 0, 200, 400, 600 and 800 s.

reveals that electrochemical activation induces dynamic reconstruction of amorphous CoB into a CoOOH/(oxy)hydroxide layer, forming a heterointerface with the metallic CoB core. Through interfacial Co-O-Co bonding, this oxyhydroxide phase extracts electrons from metallic Co sites, elevating their oxidation state to optimize oxygen intermediate adsorption and reduce OER energy barriers [46,47].

The corrosion polarization curves of amorphous CoB and crystalline CoB were tested in a 1 M KOH solution, further demonstrating the superior corrosion resistance and stability of amorphous CoB (Fig. 5**d**). Corrosion current and voltage are essential parameters for evaluating the corrosion resistance of materials. A higher corrosion voltage reflects a lower susceptibility to corrosion, while a lower corrosion current indicates a reduced corrosion rate [48]. Amorphous CoB (0.78 V vs. Ag/AgCl) and crystalline CoB (0.66 V vs. Ag/AgCl) have similar corrosion voltages, but the corrosion current of amorphous CoB (2.6 μA) is much lower than that of crystalline CoB (5.2 μA) (Fig. 5**e**). Thus, these findings convincingly demonstrate the superior corrosion resistance of the amorphous CoB electrode compared to its crystalline counterparts.

The surface activation energy (E_a) refers to the average energy barrier of the overall reaction pathway and indirectly reflects the intrinsic activity of the electrocatalyst [49]. The activation energy was calculated using the Arrhenius equation, $\ln k = \frac{-E_a}{RT} + c$, where k represents the reaction rate, R is the molar gas constant, and T is the absolute temperature [50,51]. To explore the kinetic factors enhancing the OER catalytic activity of the samples, E_a was calculated from linear sweep voltammetry polarization curves measured between 313 K and 343 K. Generally, reactants require kinetic energy exceeding the activation barrier to form products. As shown in **Fig. S14**, increasing the reaction temperature from 313 K to 343 K engages more reactants, resulting in significantly lower overpotentials for the OER reactions of both amorphous and crystalline CoB at a current density of 10 mA cm^{-2}. Specifically, the overpotential of amorphous CoB dropped from 326 mV at 313 K to 294 mV at 343 K, while that of crystalline CoB decreased from 347 mV at 313 K to 312 mV at 343 K. Activation energies at various overpotentials were derived from the slopes of linear plots, revealing that E_a for amorphous CoB was consistently lower than for crystalline CoB, aligning with theoretical predictions (Fig. 5**c**). At an overpotential of 320 mV, E_a for amorphous CoB is 17.8 kJ mol^{-1}, compared to 19.5 kJ mol^{-1} for crystalline CoB. This outcome indicates that the amorphous CoB has a significantly lower energy barrier, with its disordered, defect-rich structure reducing the kinetic energy barrier and enhancing intrinsic activity, thus leading to superior OER electrocatalytic performance [52,53].

The gas volumes of hydrogen and oxygen generated during the reaction were collected using an H-type electrolysis cell, and the hydrogen and oxygen production efficiencies were evaluated using Faraday efficiency under 1.0 M KOH conditions. The experimental setup, shown in Fig. 5**f**, includes water electrolysis tanks separated by a Nafion membrane. The O_2 produced was collected in an orange cylinder, while the H_2 was collected in a yellow cylinder. The changes in cylinder scale were recorded at 200-second intervals once the electrolysis process stabilized. By comparing the experimentally collected gas volumes with theoretical calculations, the Faraday efficiency of amorphous CoB was determined to approach 100 % for both the HER and OER (Fig. 5g and S15). Anion-exchange membrane water electrolyzer (AEMWE) testing under industrial conditions (50 mA cm^{-2}, 60°C) demonstrates practical viability. The amorphous CoB-assembled AEMWE electrolytic cell exhibited good catalytic activity and had an attenuation rate of only 4 % after 100 h of stable operation at 50 mA cm^{-2} (**Fig. S16**). These findings reveal the material's remarkable capabilities in hydrogen production, demonstrating its strong potential for practical applications in intermittent energy storage.

4. Conclusions

In summary, we present a novel magnetic field-assisted method for an amorphous cobalt boride (CoB) catalyst with a unique nanobead architecture, subsequently converted into a crystalline phase via simple thermal treatment. This innovative approach enhances active site exposure and promotes efficient electrolyte infiltration and diffusion during the oxygen evolution reaction (OER), resulting in remarkable catalytic performance. The amorphous CoB catalyst exhibits a low overpotential of 350 mV at 10 mA cm^{-2} and demonstrates superior long-term stability, maintaining performance over 100 h. Notably, in situ Raman spectroscopy reveals that the amorphous CoB undergoes rapid self-reconstruction into an active metal (oxy)hydroxide layer upon electrochemical activation. This finding supports the hypothesis that short-range order and vacancy-rich structures can significantly enhance electrocatalytic behavior. Compared to previous studies, our catalyst offers significant reductions in overpotential and enhanced durability, underscoring its potential for efficient water oxidation. This work provides valuable insights and prospects for designing advanced OER catalysts from amorphous materials.

CRediT authorship contribution statement

Meijia Liu: Writing – original draft, Formal analysis, Data curation. **Lin Wu:** Writing – review & editing, Validation, Supervision. **Yafeng Li:** Software, Investigation. **Shuai Chen:** Software. **Yuhang Lei:** Project administration, Methodology. **Zhuang Huo:** Data curation. **Lin Tao:** Writing – review & editing, Validation, Supervision. **Lixiang Li:** Resources, Conceptualization. **Chengguo Sun:** Supervision, Resources, Conceptualization. **Han Zhang:** Writing – review & editing, Supervision, Funding acquisition. **Baigang An:** Resources, Project administration, Funding acquisition, Data curation.

Declaration of competing interest

The authors declare that they have no known competing financial interests or personal relationships that could have appeared to influence the work reported in this paper.

Acknowledgements

The authors gratefully acknowledge financial supported by the National Natural Science Foundation of China (22109061, 11972178, 51972156 and 52304330), the Nature Science Foundation of Liaoning Province (2022-BS-283), and Technology Liaoning Project Grants (601010326). Key Project supported by the Research Foundation of Education Bureau of Liaoning Province (No. JYTZD2023093), Distinguished Professor Project of Education Department of Liaoning and the Open Project Found of Key Laboratory of Energy Materials and Electrochemistry Liaoning Province are acknowledged.

Appendix A. Supplementary data

Supplementary data to this article can be found online at https://doi.org/10.1016/j.jcis.2025.137409.

Data availability

Data will be made available on request.

References

[1] Y. Duan, Z.Y. Yu, S.J. Hu, X.S. Zheng, C.T. Zhang, H.H. Ding, B.C. Hu, Q.Q. Fu, Z. L. Yu, X. Zheng, J.F. Zhu, M.R. Gao, S.H. Yu, Scaled-up synthesis of amorphous NiFeMo oxides and their rapid surface reconstruction for superior oxygen evolution catalysis, Angew. Chem. Int. Ed. 58 (44) (2019) 15772–15777.

[2] H. Gao, W. Sun, X. Tian, J. Liao, C. Ma, Y. Hu, G. Du, J. Yang, C. Ge, Amorphous-amorphous coupling enhancing the oxygen evolution reaction activity and stability of the NiFe-based catalyst, ACS Appl. Mater. Interf. 14 (13) (2022) 15205–15213.

[3] R. Lin, X. Li, A. Krajnc, Z. Li, M. Li, W. Wang, L. Zhuang, S. Smart, Z. Zhu, D. Appadoo, Mechanochemically synthesised flexible electrodes based on bimetallic metal-organic framework glasses for the oxygen evolution reaction, Angew. Chem. Int. Ed. 61 (4) (2022) e202112880.

[4] J. Gao, C. Qiu, M. Ju, S. Li, R. Yu, H. Liu, M. Hu, J. Yu, M. Hong, S. Yang, Steam-driven crystalline-amorphous coupling design of homogenous metal hydroxides for oxygen evolution reaction, Appl. Catal. B 323 (2023) 122165.

[5] S. Shen, Z. Wang, Z. Lin, K. Song, Q. Zhang, F. Meng, L. Gu, W. Zhong, Crystalline-amorphous interfaces coupling of $CoSe_2$/CoP with optimized d-band center and boosted electrocatalytic hydrogen evolution, Adv. Mater. 34 (13) (2022) 2110631.

[6] H. Han, H. Choi, S. Mhin, Y.-R. Hong, K.M. Kim, J. Kwon, G. Ali, K.Y. Chung, M. Je, H.N. Umh, Advantageous crystalline-amorphous phase boundary for enhanced electrochemical water oxidation, Energy Environ. Sci. 12 (8) (2019) 2443–2454.

[7] N. Zhou, R. Liu, X. Wu, Y. Ding, X. Zhang, S. Liang, C. Deng, G. Qin, Z. Huang, B. Chen, One-spot autogenous formation of crystalline-amorphous Ni_3S_2/$NiFeO_xH_y$ heterostructure nanosheets array for synergistically boosted oxygen evolution reaction, J. Power Sources 574 (2023) 233163.

[8] H. Lan, J. Wang, L. Cheng, D. Yu, H. Wang, L. Guo, The synthesis and application of crystalline-amorphous hybrid materials, Chem. Soc. Rev. 53 (2) (2024) 684–713.

[9] L. Ge, W. Lai, Y. Deng, J. Bao, B. Ouyang, H. Li, Spontaneous dissolution of oxometalates boosting the surface reconstruction of $CoMO_x$ (M = Mo, V) to achieve efficient overall water splitting in alkaline media, Inorg. Chem. 61 (5) (2022) 2619–2627.

[10] Y. Zhou, H.J. Fan, Progress and challenge of amorphous catalysts for electrochemical water splitting, ACS Mater. Lett. 3 (1) (2020) 136–147.

[11] B. Jiang, H. Song, Y. Kang, S. Wang, Q. Wang, X. Zhou, K. Kani, Y. Guo, J. Ye, H. Li, Y. Sakka, J. Henzie, Y. Yusuke, A mesoporous non-precious metal boride system: synthesis of mesoporous cobalt boride by strictly controlled chemical reduction, Chem. Sci. 11 (3) (2020) 791–796.

[12] H.B. Tao, L. Fang, J. Chen, H.B. Yang, J. Gao, J. Miao, S. Chen, B. Liu, Identification of surface reactivity descriptor for transition metal oxides in oxygen evolution reaction, J. Am. Chem. Soc. 138 (31) (2016) 9978–9985.

[13] J. Suntivich, K.J. May, H.A. Gasteiger, J.B. Goodenough, Y. Shao-Horn, A perovskite oxide optimized for oxygen evolution catalysis from molecular orbital principles, Science 334 (6061) (2011) 1383–1385.

[14] Y. Wang, X. Li, Z. Huang, H. Wang, Z. Chen, J. Zhang, X. Zheng, Y. Deng, W. Hu, Amorphous Mo-doped $NiS_{0.5}Se_{0.5}$nanosheets@crystalline $NiS_{0.5}Se_{0.5}$ nanorods for high current-density electrocatalytic water splitting in neutral media, Angew. Chem. Int. Ed. 62 (6) (2023).

[15] J.M.V. Nsanzimana, Y. Peng, Y.Y. Xu, L. Thia, C. Wang, B.Y. Xia, X. Wang, An efficient and earth-abundant oxygen-evolving electrocatalyst based on amorphous metal borides, Adv. Energy Mater. 8 (1) (2018) 1701475.

[16] G. Chen, Y. Zhu, H.M. Chen, Z. Hu, S.F. Hung, N. Ma, J. Dai, H.J. Lin, C.T. Chen, W. Zhou, An amorphous nickel-iron-based electrocatalyst with unusual local structures for ultrafast oxygen evolution reaction, Adv. Mater. 31 (28) (2019) 1900883.

[17] D. González-Flores, I. Sánchez, I. Zaharieva, K. Klingan, J. Heidkamp, P. Chernev, P.W. Menezes, M. Driess, H. Dau, M.L. Montero, Heterogeneous water oxidation: surface activity versus amorphization activation in cobalt phosphate catalysts, Angew. Chem. Int. Ed. 54 (8) (2015) 2472–2476.

[18] J. Liu, J. Nai, T. You, P. An, J. Zhang, G. Ma, X. Niu, C. Liang, S. Yang, L. Guo, The flexibility of an amorphous cobalt hydroxide nanomaterial promotes the electrocatalysis of oxygen evolution reaction, Small 14 (17) (2018) 1703514.

[19] P.W. Menezes, C. Panda, C. Walter, M. Schwarze, M. Driess, A cobalt-based amorphous bifunctional electrocatalysts for water-splitting evolved from a single-source lazulite cobalt phosphate, Adv. Funct. Mater. 29 (32) (2019) 1808632.

[20] X. Zou, W. Zhang, X. Zhou, K. Song, X. Ge, W. Zheng, The surface of metal boride tinted by oxygen evolution reaction for enhanced water electrolysis, J. Energy Chem. 72 (2022) 509–515.

[21] H. Xu, B. Fei, G. Cai, Y. Ha, J. Liu, H. Jia, J. Zhang, M. Liu, R. Wu, Boronization-induced ultrathin 2D nanosheets with abundant crystalline-amorphous phase boundary supported on nickel foam toward efficient water splitting, Adv. Energy Mater. 10 (3) (2020) 1902714.

[22] H. Zhou, M. Zheng, H. Tang, B. Xu, Y. Tang, H. Pang, Amorphous intermediate derivative from ZIF-67 and its outstanding electrocatalytic activity, Small 16 (2) (2020) 1904252.

[23] J. Zhu, R. Lu, F. Xia, P. Wang, D. Chen, L. Chen, J. Yu, Y. Zhao, J. Wu, S. Mu, Crystalline-amorphous heterostructures with assortative strong-weak adsorption pairs enable extremely high water oxidation capability toward multi-scenario water electrolysis, Nano Energy 110 (2023) 108349.

[24] M. Yang, M. Zhao, J. Yuan, J. Luo, J. Zhang, Z. Lu, D. Chen, X. Fu, L. Wang, C. Liu, Oxygen vacancies and interface engineering on amorphous/crystalline CrO_x-Ni_3N heterostructures toward high-durability and kinetically accelerated water splitting, Small 18 (14) (2022) 2106554.

[25] H.N. Dhandapani, R. Madhu, A. De, M.A. Salem, B. Ramesh Babu, S. Kundu, Tuning the surface electronic structure of amorphous $NiWO_4$ by doping Fe as an electrocatalyst for OER, Inorg. Chem. 62 (30) (2023) 11817–11828.

[26] S. Liu, S. Geng, L. Li, Y. Zhang, G. Ren, B. Huang, Z. Hu, J.-F. Lee, Y.-H. Lai, Y.-H. Chu, A top-down strategy for amorphization of hydroxyl compounds for electrocatalytic oxygen evolution, Nat. Commun. 13 (1) (2022) 1187.

[27] J.-T. Ren, L. Chen, H.-Y. Wang, W.-W. Tian, X.-L. Song, Q.-H. Kong, Z.-Y. Yuan, Synergistic activation of crystalline ni_2p and amorphous $NiMoO_x$ for efficient water splitting at high current densities, ACS Catal. 13 (14) (2023) 9792–9805.

[28] Y. Liu, T. Sakthivel, F. Hu, Y. Tian, D. Wu, E.H. Ang, H. Liu, S. Guo, S. Peng, Z. Dai, Enhancing the d/p-band center proximity with amorphous-crystalline interface coupling for boosted pH-robust water electrolysis, Adv. Energy Mater. 13 (11) (2023) 2203797.

[29] Y. Li, B. Huang, Y. Sun, M. Luo, Y. Yang, Y. Qin, L. Wang, C. Li, F. Lv, W. Zhang, Multimetal borides nanochains as efficient electrocatalysts for overall water splitting, Small 15 (1) (2019) 2203797.

[30] J. Lu, S. Ji, P. Kannan, H. Wang, X. Wang, R. Wang, Hydrophilic $Ni(OH)_2$@CoB nano-chains with shell-core structure as an efficient catalyst for oxygen evolution reaction, J. Alloys Compd. 844 (2020) 156129.

[31] C. Liang, P. Zou, A. Nairan, Y. Zhang, J. Liu, K. Liu, S. Hu, F. Kang, H.J. Fan, C. Yang, Exceptional performance of hierarchical Ni-Fe oxyhydroxide@NiFe alloy nanowire array electrocatalysts for large current density water splitting, Energy Environ. Sci. 13 (1) (2020) 86–95.

[32] J. Masa, P. Weide, D. Peeters, I. Sinev, W. Xia, Z. Sun, C. Somsen, M. Muhler, W. Schuhmann, Amorphous cobalt boride (Co_2B) as a highly efficient nonprecious catalyst for electrochemical water splitting: oxygen and hydrogen evolution, Adv. Energy Mater. 6 (6) (2016) 1502313.

[33] S. Li, H. Zhang, L. Wu, H. Zhao, L. Li, C. Sun, B. An, Vacancy-engineered CeO_2/Co heterostructure anchored on the nitrogen-doped porous carbon nanosheet arrays vertically grown on carbon cloth as an integrated cathode for the oxygen reduction reaction of rechargeable Zn-air battery, J. Mater. Chem. A 10 (18) (2022) 9858–9868.

[34] Q. Su, R. Sheng, Q. Liu, J. Ding, P. Wang, X. Wang, J. Wang, Y. Wang, B. Wang, Y. Huang, Surface reconstruction of RuO_2/Co_3O_4 amorphous-crystalline heterointerface for efficient overall water splitting, J. Colloid Interface Sci. 658 (2024) 43–51.

[35] H.-L. Li, Y.-Y. Wang, C.-M. Liu, S.-M. Zhang, H.-F. Zhang, Z.-W. Zhu, Enhanced OER performance of NiFeB amorphous alloys by surface self-reconstruction, Int. J. Hydrogen Energy 47 (48) (2022) 20718–20728.

[36] L. Wu, S. Li, L. Li, H. Zhang, L. Tao, X. Geng, H. Yang, W. Zhou, C. Sun, D. Ju, Modest modulation on the electronic structure of Co_9S_8 by vanadium doping for high-performance rechargeable Zn-air batteries, Appl. Catal. B 324 (2023) 122250.

[37] Y. Yang, Q. Zhou, L. Jiao, Q. Yin, Z. Li, Z. Zhang, Z. Hu, Amorphous heterogeneous NiFe-LDH@$Co(OH)_2$ supported on nickel foam as efficient OER electrocatalysts, Ionics 28 (2022) 341–351.

[38] D. Tang, Y. Ma, Y. Liu, K. Wang, Z. Liu, W. Li, J. Li, Amorphous three-dimensional porous Co_3O_4 nanowire network toward superior OER catalysis by lithium-induced, J. Alloys Compod. 893 (2022) 162287.

[39] W. Chang, B. Ning, Q. Xu, H. Jiang, Y. Hu, C. Li, Strongly coupled N-doped graphene quantum dots/Ni(Fe)O_xH_y electrocatalysts with accelerated reaction kinetics for water oxidation, Chem. Eng. J. 430 (2022) 133068.

[40] T. Wang, R. Hu, H. Wei, Z. Wei, M. Yan, Y. Yang, Crystalline-amorphous Ni_3Se_4-Ni hydroxide heterostructure as an efficient electrocatalyst for oxidation evolution reaction, Chem. Res. Chin. Univ. 39 (4) (2023) 673–679.

[41] Y. Yang, S. Wei, Y. Li, D. Guo, H. Liu, L. Liu, Effect of cobalt doping-regulated crystallinity in nickel-iron layered double hydroxide catalyzing oxygen evolution, Appl. Catal. B 314 (2022) 121491.

[42] P. Sun, X. Zheng, A. Chen, G. Zheng, Y. Wu, M. Long, Q. Zhang, Y. Chen, Constructing amorphous-crystalline interfacial bifunctional site island-sea synergy by morphology engineering boosts alkaline seawater hydrogen evolution, Adv. Sci. 11 (24) (2024) 2309927.

[43] Z. Chen, R. Zheng, M. Graś, W. Wei, G. Lota, H. Chen, B.-J. Ni, Tuning electronic property and surface reconstruction of amorphous iron borides via WP co-doping for highly efficient oxygen evolution, Appl. Catal. B 288 (2021) 120037.

[44] W. Zheng, M. Liu, L.Y.S. Lee, Electrochemical instability of metal-organic frameworks: in situ spectroelectrochemical investigation of the real active sites, ACS Catal. 10 (1) (2019) 81–92.

[45] H. Sun, L. Chen, Y. Lian, W. Yang, L. Lin, Y. Chen, J. Xu, D. Wang, X. Yang, M. H. Rümmerli, Topotactically transformed polygonal mesopores on ternary layered double hydroxides exposing under-coordinated metal centers for accelerated water dissociation, Adv. Mater. 32 (52) (2020) 2006784.

[46] R. Gan, Q. Zhao, Y. Ran, Q. Ma, G. Cheng, L. Fang, Y. Zhang, D. Wang, Regulating interfacial microenvironment via anion adsorption to boost oxygen evolution reaction, Journal of Colloid, Interface Sci. 687 (2025) 724–732.

[47] X. Zhang, H. Zhong, Q. Zhang, Q. Zhang, C. Wu, J. Yu, Y. Ma, H. An, H. Wang, Y. Zou, High-spin Co^{3+} in cobalt oxyhydroxide for efficient water oxidation, Nat. Commun. 15 (1) (2024) 1383.

[48] S. Ge, X. Shen, J. Gao, K. Ma, H. Zhao, R. Fu, C. Feng, Y. Zhao, Q. Jiao, H. Li, Synergy of Mo doping and heterostructures in $FeCo_2S_4$@Mo-NiCo LDH/NF as durable and corrosion-resistance bifunctional electrocatalyst towards seawater electrolysis at industrial current density, Chem. Eng. J. 485 (2024) 150161.

[49] Z. Lin, P. Bu, Y. Xiao, Q. Gao, P. Diao, β- and γ-NiFeOOH electrocatalysts for an efficient oxygen evolution reaction: an electrochemical activation energy aspect, J. Mater. Chem. A 10 (39) (2022) 20847–20855.

[50] M. Wang, C.L. Dong, Y.C. Huang, Y. Li, S. Shen, Electronic structure evolution in tricomponent metal phosphides with reduced activation energy for efficient electrocatalytic oxygen evolution, Small 14 (35) (2018) 1801756.

[51] L. Li, H. Yang, J. Miao, L. Zhang, H.-Y. Wang, Z. Zeng, W. Huang, X. Dong, B. Liu, Unraveling oxygen evolution reaction on carbon-based electrocatalysts: effect of

oxygen doping on adsorption of oxygenated intermediates, ACS Energy Lett. 2 (2) (2017) 294–300.
[52] C. Fan, X. Wu, M. Li, X. Wang, Y. Zhu, G. Fu, T. Ma, Y. Tang, Surface chemical reconstruction of hierarchical hollow inverse-spinel manganese cobalt oxide boosting oxygen evolution reaction, Chem. Eng. J. 431 (2022) 133829.
[53] X. Yu, B. Wang, C. Wang, C. Zhuang, Y. Yao, Z. Li, C. Wu, J. Feng, Z. Zou, 2D high-entropy hydrotalcites, Small 17 (45) (2021) 2103412.